Dynamics of multimode diode lasers with strong, frequency-selective optical feedback

R. Badii,[1] N. Matuschek,[2] T. Pliška,[2] J. Troger,[2] and B. Schmidt[2]
[1]*Physics Institute, University of Zurich, Winterthurerstrasse 190, 8057 Zurich, Switzerland*
[2]*R&D Department, Bookham Technology plc., Binzstrasse 17, 8045 Zurich, Switzerland*
(Received 13 November 2002; published 9 September 2003)

The dynamical behavior of a class of multimode semiconductor diode lasers with emission wavelength around 980 nm is investigated both experimentally and numerically in the presence of strong, frequency-selective optical feedback provided by a fiber Bragg grating. The focus is set on the switching between broad- and narrow-band optical spectra, on chaotic transitions, and on the loss of frequency locking between laser and grating. Laser and feedback parameters are chosen in the typical ranges pertaining to wavelength stabilization in erbium-doped fiber amplifiers for telecommunication applications. An improved set of rate equations, which allows for arbitrary feedback levels and includes experimentally measured gain and linewidth enhancement factor, is studied analytically and numerically.

DOI: 10.1103/PhysRevE.68.036605 PACS number(s): 42.55.Ah, 05.45.−a, 42.55.Px, 42.60.Mi

I. INTRODUCTION

Fiber-optical data transmission, based on wavelength division multiplexing and erbium-doped fiber amplifiers (EDFAs), relies on the accurate definition of the emission wavelengths of the lasers it employes. These essentially accomplish two tasks: emitting the signal (in the 1520–1570 nm and 1570–1620 nm regions) and amplifying it by pumping the erbium atoms in the EDFAs (in absorption bands center around 980 nm and 1480 nm).

Two different kinds of frequency selection and stabilization, corresponding to the two above-mentioned tasks, stand out. The former aims at realizing narrow-band laser sources; the latter, multimode emission with a bandwidth ($\lesssim 3$ nm) that matches the absorption spectrum of the erbium as closely as possible within a broad operating-temperature interval.

In both cases, stability and high out-of-band power suppression are of primary importance. They need to be achieved and maintained against fluctuations in the device characteristics arising from the fabrication processes and drifts in the gain curve induced by temperature or current variations.

Effective wavelength selection can be obtained with distributed feedback and distributed Bragg reflector lasers, which are the appropriate sources for signal transmission. Fiber Bragg gratings (FBGs), on the other hand, have established themselves as the preferred tools for pump lasers (which are employed in the amplification of the signals), because of their superior wavelength stabilization properties, versatility, good manufacturability, and low cost.

Depending on the design characteristics of the devices (laser and FBG) and on their mutual distance, a variety of phenomena can be observed. In addition to providing the desired spectral bandwidth reduction and locking of the emission spectrum to the FBG's central frequency [1–3], the feedback may break the temporal stability of the electromagnetic field [4–6]. In fact, the signal reflected from the FBG interferes with the internal field of the laser after the round trip time in the fiber (the ''external cavity''), thus providing a further time scale to the dynamics [7]. This generates power fluctuations (in time and upon change of control parameters [14,15]), broadening of the optical spectrum (up to several gigahertz: hence, the name of ''coherence collapse'' assigned to this regime [16,17]), or even loss of the frequency locking.

In the present paper, we discuss experimental results illustrating the switching between broad- and narrow-band optical spectra in 980-nm pump lasers of different generations, when they are coupled to a fiber Bragg grating with typical configuration parameters for optical communication applications [18]. In particular, we focus on the case in which the ratio between the grating's and the laser's front-facet reflectivity is too large for a realistic application of the low-feedback approximations usually considered in the literature. The lasers are of the single-quantum-well, ridge-waveguide type.

Our theoretical description is based on an improved set of rate equations, which allows for arbitrary, frequency-selective feedback levels; moreover, we include experimentally measured gain and linewidth enhancement factors, accounting for temperature- and current-induced drifts.

The large-feedback, long-cavity regime in which we operate lies well beyond the region in which the system first becomes chaotic (usually via the quasiperiodic route). Therefore, the bifurcation analysis of the laser's output upon increase of the feedback amplitude and in dependence of the delay time is of little utility for the understanding of the dynamics. The system finds itself deeply in a chaotic region of parameter space and admits multistable behavior which includes coexistence of chaotic attractors. This phenomenology has no counterpart in single-mode models.

We show that the switching between broad- and narrow-band optical spectra corresponds to transitions between coexisting chaotic and stable periodic attractors in phase space and is inherently different from the coherence-collapse low-frequency fluctuations (LFF) that occur in single-mode models as well. In the multimode case, in fact, such fluctuations are usually consistent with broadband optical spectra [19]: different modes oscillate with different relative phases and the spectra, averaged over a delay time, appear quite stable despite the intermittency of some individual modes' amplitudes. No single-mode chaotic motion has been observed,

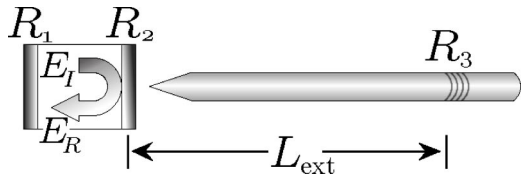

FIG. 1. Schematic representation of the laser diode, confined within the two reflectors R_1 and R_2, and of the external fiber Bragg grating R_3 with indication of incident and reflected field at the front facet.

except for extremely narrow-bandwidth FBG reflectivity and low current.

Finally, the loss of frequency locking is associated with considerable changes of the carrier density, the speed of which is essentially given by the relaxation frequency of the laser. Since this is much larger than the average frequency of the LFFs, the mode's amplitudes change very little within this time frame and the instability presents itself, in phase space, as an oscillatory motion ''transversal'' to the direction of the LFFs.

II. MODEL EQUATIONS

The derivation of the model can be followed with reference to Fig. 1, which illustrates the experimental setup with the diode laser, confined between the two reflectors R_1 and R_2, and the fiber Bragg grating R_3 [20], inscribed in the glass fiber at a distance $L_{\rm ext}$ from the laser's front facet R_2. The relevant variables are the carrier density $N(t)$ and the slowly varying modal amplitudes $\sqrt{P_n(t)}$ and phases $\phi_n(t)$ of the complex field

$$E_I(t)=\sum_n \sqrt{P_n(t)}e^{i[\nu_n t+\phi_n(t)]} \tag{2.1}$$

incident into the front facet R_2 from inside the laser. The squared amplitude P_n is proportional to the optical intensity of the nth longitudinal mode. The instantaneous frequency of the nth mode is given by

$$\omega_n=\nu_n+\dot{\phi}_n. \tag{2.2}$$

At resonance, the reference value ν_n can be assumed to coincide with one of the Fabry-Perot frequencies

$$\Omega_n=\Omega_0(I)+n(\Delta\Omega) \quad (n\in\mathbb{Z}), \tag{2.3}$$

where $\Omega_0(I)$ is the frequency of the central mode at the current I and $\Delta\Omega$ is the mode spacing.

The reflected complex field $E_R(t)$ inside the laser at the mirror R_2 is the superposition of the first simple reflection at R_2 and of multiple reflections between R_2 and the grating R_3. Labeling with $\ell=1,2,\ldots$ the successive round trips in the external cavity, the generic component $\mathcal{E}_R$ of E_R at the frequency ω, can be written as

$$\mathcal{E}_R(t)=r_2\left[\mathcal{E}_I(t)+F(\omega)\sum_{\ell=1}^{\infty}[-r_2r_3(\omega)]^{\ell-1}\mathcal{E}_I(t-\ell T)\right], \tag{2.4}$$

where $\mathcal{E}_I$ is the corresponding component of the incident field, r_2 is the reflection coefficient at the front facet R_2, $r_3(\omega)$ is the complex reflection coefficient of the FBG, and T is the round trip time in the external cavity. For simplicity, we choose $r_2=\sqrt{R_2}>0$ real and frequency independent. The feedback amplitude term $F(\omega)$ is defined as

$$F(\omega)=\eta_{\rm F}\frac{1-r_2^2}{r_2}r_3(\omega), \tag{2.5}$$

where η_F is the power coupling efficiency between laser and fiber. The form of $r_3(\omega)$ is characterized by the central wavelength $\lambda_{\rm Bragg}$ and the width $\Delta\lambda$ (between the two minima adjacent to $\lambda_{\rm Bragg}$) [21]: in our case, it describes a uniform, nonapodized FBG. Since $r_2|r_3(\omega)|\ll 1$, higher-order reflections will be neglected in the following. Generally, they can be taken into account in a simple way only when the variation of the field across a delay time T is negligible, so that $\mathcal{E}_I(t-\ell T)/\mathcal{E}_I[t-(\ell+1)T]\approx\mathcal{E}_I[t-(\ell+1)T]/\mathcal{E}_I[t-(\ell+2)T]$ and the series in Eq. (2.4) admits an analytic sum (a similar, albeit additive, approximation was proposed in Refs. [22]). The ratio

$$r_{\rm eff}(\omega)=\frac{\mathcal{E}_R(t)}{\mathcal{E}_I(t)} \tag{2.6}$$

can now be taken as the definition of an effective reflection coefficient for the compound (R_2,R_3). Specializing to the mode-n component, and dividing by r_2, we have

$$\frac{r_{\rm eff}(\omega_n)}{r_2}=1+F(\omega_n)\sqrt{\frac{P_n(t-T)}{P_n(t)}}e^{-i[\nu_nT+\phi_n(t)-\phi_n(t-T)]}. \tag{2.7}$$

In order to include the effect of the grating into the rate equations, $r_{\rm eff}$ is substituted for r_2 into the mirror loss coefficient

$$\alpha_M=-\frac{1}{L}\ln(r_1r_2) \tag{2.8}$$

to yield the effective field decay rate

$$\gamma_{\rm eff}=v_{\rm gr}\left[\alpha_I-\frac{1}{L}\ln(r_1r_{\rm eff})\right] \tag{2.9}$$

of the compound cavity, where L is the laser's cavity length, $v_{\rm gr}$ is the group velocity, and α_I is the internal loss coefficient. Clearly, $\gamma_{\rm eff}$ is the sum of the solitary laser's decay rate

$$\gamma=v_{\rm gr}[\alpha_I+\alpha_M], \tag{2.10}$$

and of the cavity loss

$$\gamma_n' = -\frac{v_{gr}}{L}\ln\frac{r_{eff}(\omega_n)}{r_2}. \quad (2.11)$$

These expressions, specified for each frequency ω_n, are then inserted into the field's rate equations [23]

$$\dot{E}_n = \left[i\Omega_n + \frac{1}{2}(G_n - \gamma)(1 + i\alpha_n) - \frac{\gamma_n'}{2}\right] E_n, \quad (2.12)$$

where $G_n = G(\omega_n)$ is the stimulated emission at ω_n and $\alpha_n = \alpha(\omega_n)$ is the (frequency-dependent) linewidth enhancement factor [24]. Recalling Eq. (2.1) and separating real (Re) and imaginary (Im) part of the field yields

$$\dot{P}_n = [G_n - \gamma - \mathrm{Re}(\gamma_n')]P_n + S_n G_n, \quad (2.13)$$

$$\dot{\phi}_n = \frac{\alpha_n}{2}[G_n - \gamma] - \frac{\mathrm{Im}(\gamma_n')}{2},$$

in which the spontaneous emission S_n has been introduced phenomenologically.

The stimulated emission term is expressed as

$$G_n = \frac{H g_n}{1 + \epsilon P_n}\ln\frac{N}{N_{tr}}, \quad (2.14)$$

where $H = v_{gr}\Gamma g_{max}$, Γ is the modal confinement factor, g_{max} is the maximum of the gain curve $g(\omega)$, $g_n = g(\omega_n)/g_{max} < 1$ the rescaled gain, ϵ is the gain compression factor [25], N is the carrier density, and N_{tr} its transparency value. The rate equations (2.13) are completed by the derivative

$$\dot{N} = \frac{\eta_I I}{|e|V} - AN - BN^2 - CN^3 - \frac{1}{\Gamma}\sum_n G_n P_n \quad (2.15)$$

of the carrier density, where η_I is the internal efficiency, $|e|$ is the electron charge, V is the volume of the active region, and A, B, and C are the nonradiative, spontaneous, and Auger recombination coefficients, respectively.

In the simulation, analytical fits to experimental values of $\alpha(\omega)$ and $g(\omega)$ have been used.

Linewidth enhancement and gain measurements. The Fabry-Perot lasers investigated in this work are based on the InGaAs/AlGaAs material system. Their graded-index carrier confinement with a single quantum well is grown by molecular beam epitaxy. The narrow-stripe ridge waveguide provides lateral confinement to the fundamental optical mode. We consider several generations of devices, differing in epitaxial structure, waveguide design, and cavity length [26]. The light is coupled into a single-mode fiber by means of a lens polished on the fiber tip. Coupling efficiencies between 0.75 and 0.84 are obtained.

In semiconductor lasers, the coupling between the carrier-induced variation of the refractive index and the gain is expressed by the linewidth enhancement factor $\alpha(\omega)$ [24]. Its magnitude was estimated experimentally by measuring the gain and the Fabry-Perot mode shift as a function of the current density below and above threshold, and using the method described in Ref. [27]. The resulting curve, obtained at a heat-sink temperature of 25 °C, is shown in Fig. 2.

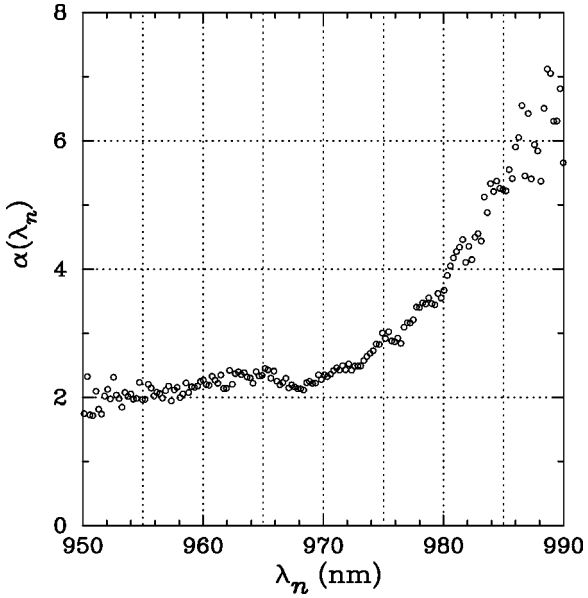

FIG. 2. Experimental values of the linewidth enhancement factor $\alpha(\lambda)$ vs the wavelength λ in nm, measured at 25 °C.

The modal net gain was estimated from the spontaneous emission spectra of the diode laser (TE polarization) using the method described in Ref. [28] by Cassidy. For comparison, we also applied the more commonly used method by Hakki and Paoli [29]. The former is more appropriate in our case because of its weaker dependence on the wavelength resolution of the measurement system. Figures 3(a) and 3(b) show the gain curves of a Fabry-Perot pump laser as a function of the emission wavelength. In Fig. 3(a), the heat-sink temperature was held fixed at 25 °C and the current was chosen as 0.42, 0.55, 0.83, and 1.05 times its threshold value (from bottom to top). In Fig. 3(b), with the current at threshold, the following temperatures were chosen: 15, 25, 35, 45, 55, 65, and 75 °C (from left to right in the figure). As the temperature increases, the gain curves are seen to shift to longer wavelength (temperature- and carrier-induced band gap reduction) and to broaden (due to enhanced carrier spreading inside the bands). The threshold current density increases accordingly.

The drifts of the gain curve towards larger wavelengths upon increase of both driving current and device temperature have been incorporated into the model via suitable fit functions.

III. RESCALING AND FIXED-POINT SOLUTIONS

In order to simplify the analysis, it is convenient to introduce the adimensional variables

$$x_n = \frac{H}{AN_{tr}\Gamma}P_n, \quad y = \frac{N}{N_{tr}}, \quad t = Ht_{ph}, \quad (3.1)$$

where t_{ph} is the physical time and t the new rescaled time. In the following, all time derivatives will be taken with respect to t. By further defining

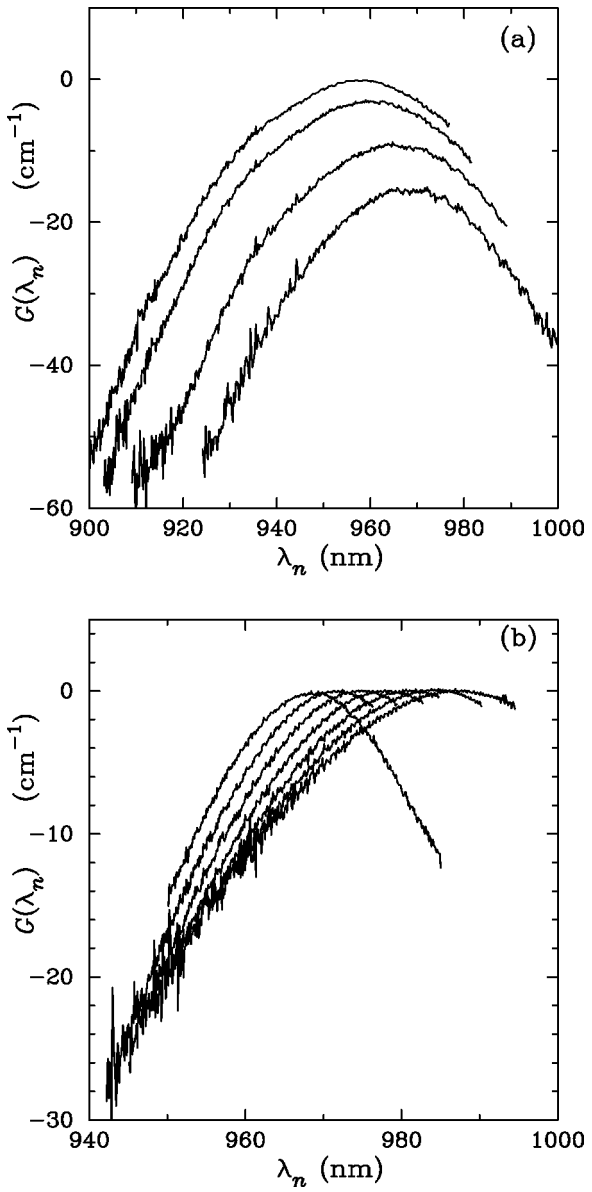

FIG. 3. Experimentally measured gain $G(\lambda_n)$ per centimeters as a function of the wavelength λ_n (in nanometers) for a 980-nm diode laser. In (a), the temperature was held at 25 °C and the current varied from 0.42 to 1.05 times the threshold value (from bottom to top); in (b), seven different temperatures (increasing from left to right) were selected at threshold. More details are provided in the text.

$$k=\frac{\gamma}{H},\quad s_n=\frac{H}{AN_{\rm tr}\Gamma}S_n,$$

$$J=\frac{\eta_I}{eVAN_{\rm tr}}I\equiv\frac{I}{I_0},\quad \varepsilon=\frac{AN_{\rm tr}\Gamma}{H}\epsilon,$$

$$a=\frac{A}{H},\quad b=\frac{B}{A}N_{\rm tr},\quad c=\frac{C}{A}N_{\rm tr}^2, \tag{3.2}$$

$$\rho_n=\frac{\mathrm{Re}(\gamma_n')}{H},\quad \sigma_n=\frac{\mathrm{Im}(\gamma_n')}{H},$$

the laser equations can be rewritten as

$$\dot{x}_n=-(k+\rho_n)x_n+g_n\frac{s_n+x_n}{1+\varepsilon x_n}\ln y,$$

$$\dot{\phi}_n=\frac{\alpha_n}{2}\left(\frac{g_n\ln y}{1+\varepsilon x_n}-k\right)-\frac{\sigma_n}{2}, \tag{3.3}$$

$$\dot{y}=a\left[J-y-by^2-cy^3-\sum_n\frac{g_nx_n\ln y}{1+\varepsilon x_n}\right].$$

The rescaled real and imaginary parts of the cavity loss γ', ρ_n, and σ_n, contain the rescaled round trip time

$$\tau=HT \tag{3.4}$$

in the external cavity.

The following numerical values can be assumed for reference purposes, although they vary for the laser generations we have investigated:

$$H=2.8\times10^{11}\ \ \mathrm{s}^{-1},$$

$$I_0=9\times10^{-3}\ \ \mathrm{A},$$

$$k=0.4,$$

$$\max\{|s_n|\}=5\times10^{-5}, \tag{3.5}$$

$$\varepsilon=8.5\times10^{-4},$$

$$a=7\times10^{-4},$$

$$b=0.7,$$

$$c=0.06.$$

Generation-II lasers are 33% longer than generation-I lasers. In addition, the front-facet reflectivity R_2 of generation-II lasers is 38% smaller. However, these differences have only a minor effect on the value of k. The main change occurs in the feedback amplitude $F(\omega)$, where R_2 appears in the denominator, which improves the locking capability of generation-II lasers in the external cavity.

A. Fixed points

Generally, Eqs. (3.3) admit a fixed-point solution in the variables x_n and y only, but not in the phases ϕ_n. In fact, the presence of the feedback induces a net constant contribution θ_n to $\dot{\phi}_n$, which brings the instantaneous frequencies (2.2) closer to nearby modes of the external cavity: the remaining difference is accounted for by the slowly varying part

$$\psi_n(t)=\phi_n(t)-\theta_nt. \tag{3.6}$$

Accordingly, the arguments of the complex exponential in Eq. (2.7) can be rewritten (in rescaled units) as

$$\Phi_n+\phi_n(t)-\phi_n(t-\tau)=\Phi_n+\theta_n\tau+\psi_n(t)-\psi_n(t-\tau), \tag{3.7}$$

where $\Phi_n = \nu_n T \bmod 2\pi$. The new variables ψ_n do admit fixed-point solutions.

Therefore, we indicate with $(\{x_n^0\},\{\psi_n^0\},y_0)$ the solutions of $(\dot{x}_n,\dot{\psi}_n,\dot{y})=0$ in Eqs. (3.3) and write the steady-state mode amplitudes as

$$x_n^0 = \frac{(r_n \ln y_0 - 1) + \sqrt{(r_n \ln y_0 - 1)^2 + 4\varepsilon r_n s_n \ln y_0}}{2\varepsilon}, \tag{3.8}$$

where

$$r_n = g_n/(k+\rho_n) \tag{3.9}$$

is the ratio between gain and loss for mode n (the superscript 0 having been omitted from r_n, s_n, and ρ_n, for simplicity). Although the value of y_0 cannot be computed analytically, since this requires solving transcendental equations, the approximate estimate

$$\ln y_0 = \frac{1+\varepsilon x_n}{r_n} + O(s_n) \tag{3.10}$$

is readily obtained from the first of Eqs. (3.3): the symbol $O(s_n)$ represents a first-order correction in s_n. This expression immediately allows one to separate lasing from nonlasing modes:

$$x_n \gtrsim O(\varepsilon)/\varepsilon, \quad \text{if } r_n \ln y_0 > 1 + O(\varepsilon), \tag{3.11}$$

$$x_n \lesssim O(\sqrt{s_n/\varepsilon}), \quad \text{if } r_n \ln y_0 < 1 - O(\varepsilon).$$

Therefore, since $y_0 > 1$ is hardly larger than 2 in most practical applications, the gain/loss ratio r_n must be sufficiently large for mode n to be lasing.

We further use Eq. (3.10) to eliminate x_n from the last of Eqs. (3.3) for $\dot{y}=0$ and restrict the sum to the set $N_+ = \{n: g_n > 0\}$: these, in fact, are the labels of the only modes with a chance of overcoming the threshold $J_{\rm th}$, which can be defined as

$$J_{\rm th} = y_0 + b y_0^2 + c y_0^3. \tag{3.12}$$

By setting $n_+ = \mathrm{card}(N_+)$ and

$$\Delta = J - J_{\rm th}, \tag{3.13}$$

we finally obtain

$$\ln y_0 = \left(k + \overline{\rho}_+ + \frac{\Delta\varepsilon}{n_+} \right) / \overline{g}_+, \tag{3.14}$$

where $\overline{O}_+ = \Sigma_{N_+} O_n / n_+$ denotes the average of the generic mode observable O_n in the positive-gain range N_+. This expression yields the fixed-point solution for the carrier density. Upon neglection of the third term on the right-hand side (rhs) of Eq. (3.14) and insertion into Eq. (3.12), an explicit expression for the threshold current can be obtained. The term $\overline{\rho}_+$, however, still contains the phases ψ_n^0, which will be discussed in the following.

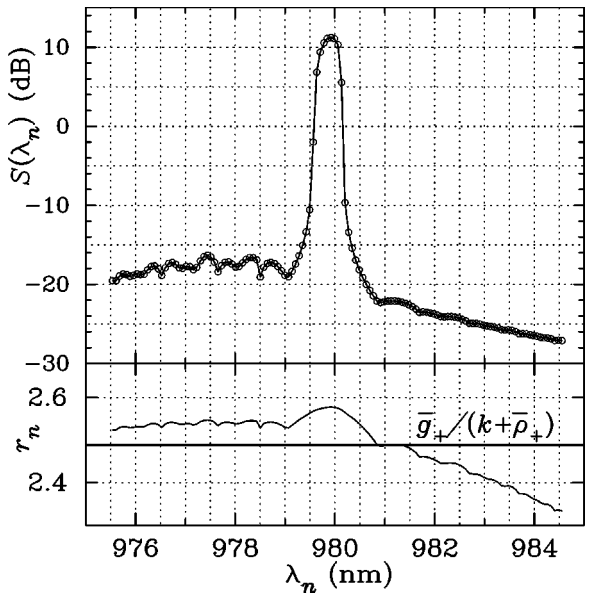

FIG. 4. Numerical optical spectrum $S(\lambda_n)$ (upper panel, decibels) and gain/loss ratio r_n (lower panel) vs the wavelength λ_n in nanometers. The parameter values used in the simulation are reported in the text.

The lasing condition (3.11) can be rephrased as

$$r_n \ln y_0 = \frac{g_n}{\overline{g}_+} \frac{k+\overline{\rho}_+}{k+\rho_n} \gtrsim 1, \tag{3.15}$$

up to a term of the order of $\Delta\varepsilon/n_+$. For the free-running laser ($\rho_n = 0$), this implies that the lasing modes are those having a gain g_n that lies above the average $\overline{g}_+$. The general case with $\rho_n \neq 0$ is illustrated in Fig. 4 for $I = 120$ mA, $L_{\rm ext} = 0.5$ m, $R_3 = 0.0001$, and a fiber Bragg grating bandwidth $\Delta\lambda = 2$ nm. The horizontal line in the lower panel represents the ratio between the average gain and the average loss in N_+.

B. Phase behavior in the Lang-Kobayashi approximation

The phase dynamics is better discussed with reference to a simplified model, proposed by Lang and Kobayashi in Ref. [4], which can be recovered from Eqs. (3.3), (2.11), and (2.7) in the weak-feedback limit $\max\{|r_3|\}/r_2 \ll 1$. By expanding the logarithm in Eq. (2.11) for $F(\omega_n) \ll 1$ and setting

$$f_n = \frac{v_{\rm gr}}{HL} F(\omega_n), \tag{3.16}$$

the first two equations in Eqs. (3.3) take the form

$$\dot{x}_n = -k x_n + g_n \frac{s_n + x_n}{1+\varepsilon x_n} \ln y + f_n \sqrt{x_n x_n'} \cos[\Phi_n + \phi_n - \phi_n'] \tag{3.17}$$

$$\dot{\phi}_n = \frac{\alpha_n}{2} \left(\frac{g_n \ln y}{1+\varepsilon x_n} - k \right) - \frac{f_n}{2} \sqrt{\frac{x_n'}{x_n}} \sin[\Phi_n + \phi_n - \phi_n'],$$

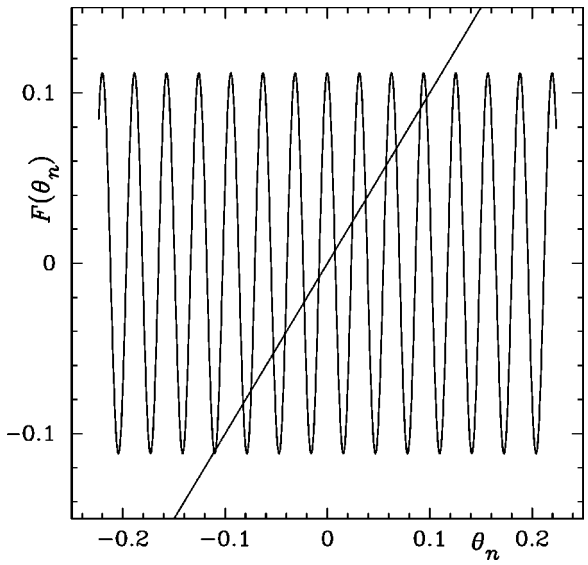

FIG. 5. Illustration of the fixed-point relation (3.21) for the phase shift in the Lang-Kobayashi model: the symbol $F(\theta_n)$ denotes the function on the rhs of Eq. (3.21).

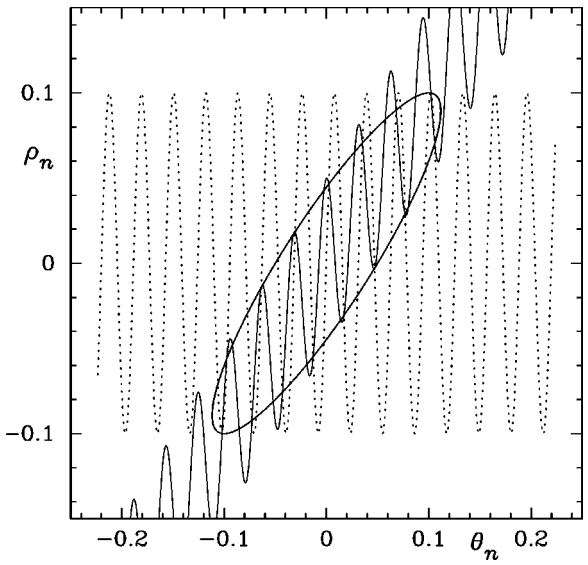

FIG. 6. The three curves ρ_n (real part of the compound-cavity loss) vs θ_n (feedback-induced modal frequency shift) that correspond to the Lang-Kobayashi fixed-point conditions in Eqs. (3.19) (thin, solid), (3.20) (dotted), and (3.22) (ellipse).

where the prime in x_n' and ϕ_n' indicates that these values are taken at the delayed time $t-\tau$. With the addition of the equation for the carrier density, which is unchanged from Eqs. (3.3), these are the Lang-Kobayashi equations, in adimensional form.

At the fixed point, $x_n=x_n'$, $\phi_n=\phi_n'+\theta_n\tau$, and $\dot{\phi}_n=\theta_n$: using Eq. (3.10), rewritten as

$$\frac{g_n \ln y_0}{1+\varepsilon x_n}-k=\rho_n+O(s_n), \tag{3.18}$$

the second of Eqs. (3.17) becomes

$$\theta_n=\frac{\alpha_n}{2}\rho_n-\frac{f_n}{2}\sin[\Phi_n+\theta_n\tau], \tag{3.19}$$

where the small-feedback expansion

$$\rho_n=-f_n\cos(\Phi_n+\theta_n\tau) \tag{3.20}$$

can be applied. A simple trigonometric operation finally yields

$$\theta_n=-\frac{f_n}{2}\sqrt{1+\alpha_n^2}\sin[\Phi_n+\theta_n\tau+\arctan(\alpha_n)]. \tag{3.21}$$

Therefore, a complete fixed-point solution for the (small-feedback) rate equations can be found only if each modal frequency ω_n is displaced from its solitary-laser value ν_n [see Eq. (2.2)] by the amount θ_n that solves Eq. (3.21). It may be noticed that this result is exact in ε.

Multiple solutions exist if the derivative of the rhs of Eq. (3.21) is larger than 1 at the inflection points, i.e., if $f_n\tau\sqrt{1+\alpha_n^2}/2>1$. This is illustrated in Fig. 5, for $f_n=0.1$, $\alpha_n=2$, and $\tau=200$ [the label $F(\theta_n)$ denotes the rhs of Eq. (3.21)]. The values of f_n and τ are usually larger ($\tau>2000$): the number of fixed points increases and their separation decreases accordingly. Furthermore, Eqs. (3.19) and (3.20) can be combined into the form

$$(2\theta_n-\alpha_n\rho_n)^2+\rho_n^2=f_n^2, \tag{3.22}$$

which defines an ellipse in the plane (θ_n,ρ_n). The three curves ρ_n versus θ_n defined by Eqs. (3.19), (3.20), and (3.22) are displayed in Fig. 6. Their intersections determine the fixed points of the system. For large feedback, the analytical study is considerably more difficult. The locations of the fixed points are still found on approximately elliptic curves, for moderate values of R_3, but strong deformations appear for large R_3.

The potential number of solutions is very large: if n_0 modes are comprised within the FBG's bandwidth, and each of them exhibits m intersections in Eq. (3.21), we may expect about m^{n_0} different solutions. Therefore, a stability analysis of this system cannot be easily carried out analytically. Nevertheless, results obtained for the single-mode case [5,30,31] are still qualitatively valid. In particular, solutions located in the lower part of the ellipse correspond to modes of the compound cavity and are stable for weak feedback; solutions on the upper branch are always unstable. The phase shifts θ_n are of the order of 1/4–1/2 of the mode separation $\Delta\Omega$ (2.3).

For increasing feedback level, several structural changes occur, which include Hopf bifurcations of fixed points and limit cycles, with the creation of tori, torus breakup, intermittency, and crises. Because of the low front-facet reflectivity R_2 in optical communications equipment, chaotic behavior is already achieved for $R_3\gtrsim 10^{-4}$ and the large-feedback regime can be defined by $R_3\gtrsim 10^{-2}$ (the coupling efficiency η_F being of the order of 0.75–0.84). Therefore, in these applications, the Lang-Kobayashi model is incorrect even though simulations have been presented in the literature in which it was used with parameter values outside of its valid-

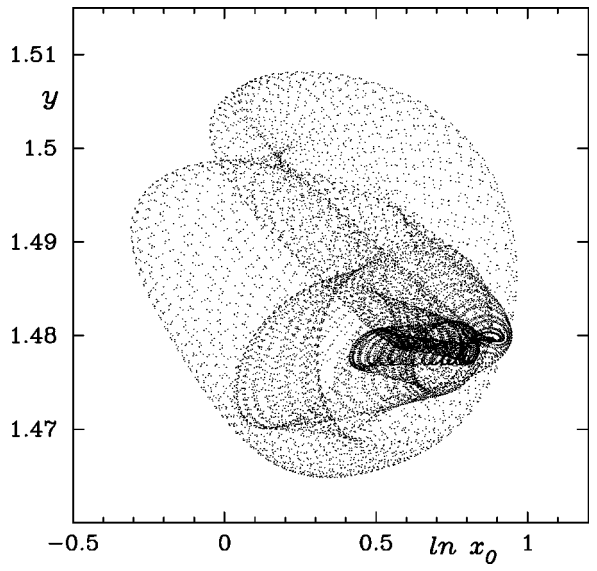

FIG. 7. Numerical attracting torus at $I=50$ mA, $R_3=0.000\,15$, $L_{\rm ext}=0.25$ m, and $\Delta\lambda=1$ nm. This attractor coexists with at least two stable fixed points, with coordinates $(\ln x_0,y)$ close to $(-4.167,1.4782)$ and $(0.842,1.47915)$ in this projection.

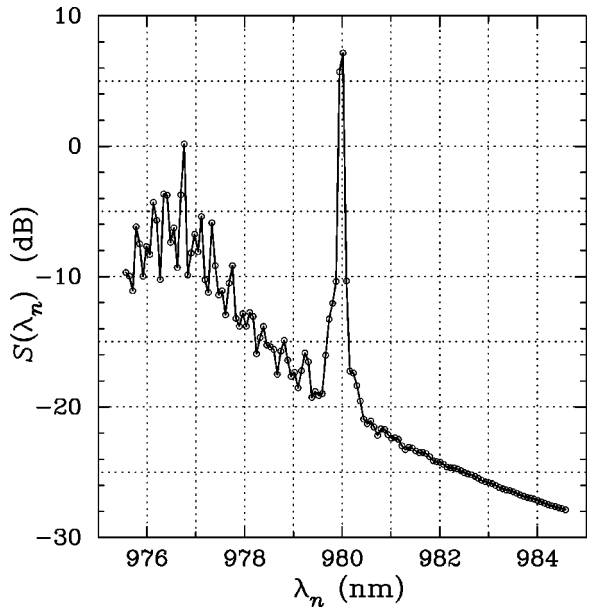

FIG. 8. Numerically computed optical spectrum $S(\lambda)$ vs λ (in nanometers), averaged over a delay time τ, for the solution of Fig. 7. The spectrum is in a $10\log_{10}$ scale, computed using the adimensional variables x_n and including the proper transmission factors through both R_2 and R_3. All numerical spectra are prepared in this way.

ity range. In particular, the phenomenology in the large-feedback regime can only be studied with model (3.3). A few solutions observed in these regions of the parameter space will be illustrated in the following section.

IV. MAIN TRAJECTORIES AND TRANSITION TYPES

System (3.3) has been integrated by using 128 or 256 laser modes and phases, correcting the sum in the third equation in Eqs. (3.3) to account for the amplitudes of the excluded side modes. The logarithms $q_n=\ln x_n$ of the mode amplitudes have been integrated, rather than the x_n themselves, to achieve a higher accuracy. Because of the widespread multistability of this system, we illustrate a few samples of its typical behavior, rather than scanning a portion of parameter space in a systematic manner. In the following, we present four main types of solutions or transitions: a quasiperiodic attractor, a transient from a narrow band to a multimode optical spectrum, coexisting strange attractors, and the alternation between well-locked and partly locked spectra. While the first is shown only for illustration purposes, the other three situations are typical of these systems and relevant for the applications.

At very low feedback, fixed points are the most common solution. Their bifurcations, however, are quite abrupt and hard to follow. Therefore, limit cycles and tori are seldom observed. In Fig. 7, an attracting torus is shown in a two-dimensional projection of phase space: the horizontal axis corresponds to the logarithm of the 980 nm mode amplitude x_0, and the vertical one to the normalized carrier density y. The relevant parameters values are $I=50$ mA, $R_3=0.000\,15$, $L_{\rm ext}=0.25$ m, and $\Delta\lambda=1$ nm. The two main frequencies correspond to the relaxation oscillations and to the round trip in the external cavity: their ratio is ≈ 3.636. It should be pointed out that this solution coexists with at least two stable fixed points, the coordinates $(\ln x_0,y)$ of which are close to $(-4.167,1.4782)$ and $(0.842,1.47915)$ in this two-dimensional subspace. Of course, coexistence of (possibly many) more attractors is not excluded. The optical spectrum corresponding to the torus of Fig. 7 is shown in Fig. 8: an average over a delay time τ has been taken in order to obtain a stable picture which can be compared with the experimental ones. The spectra of the two fixed points are similar: the former has a dip at $\lambda_0=980$ nm and the latter has one at the nearby lower-wavelength mode. Tori first appear after the solitary laser's fixed point has undergone two Hopf bifurcations (first, to a limit cycle and, then, to a torus) upon gradual increase of the external reflectivity R_3. The extremely low value of R_3 shows how ''compressed'' the bifurcation region is with respect to the domain in which commercial devices operate.

A chaotic transition with a broadening of the optical spectrum is illustrated in Figs. 9–11 which all refer to the following parameter values: $I=120$ mA, $R_3=0.015$, $L_{\rm ext}=1$ m, and $\Delta\lambda=2$ nm. A transient orbit, corresponding to about 600 roundtrips in the external cavity, eventually evolves into the globally stable strange attractor in Fig. 10. The respective optical spectra, also averaged over a time τ, are qualitatively different (single-mode vs multimode: see Fig. 11). Notice the smoothness of the multimode spectrum, in spite of the irregular shape of the attractor in Fig. 10, with its bursts into both low-amplitude x_0 and high carrier density y regions. At nearby parameter values, stable single- or two-mode solutions are found, which correspond to fixed points in phase space, although they are difficult to locate because of the smallness of their basins of attraction. Noise can destabilize them and cause the alternation between narrow and multi-

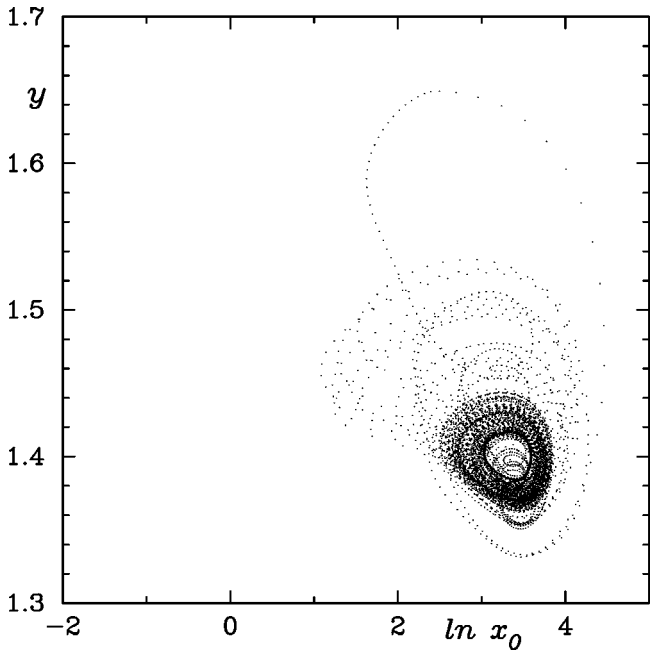

FIG. 9. Metastable chaotic orbit, computed at $I=120$ mA, $R_3=0.015$, $L_{\text{ext}}=1$ m, and $\Delta\lambda=2$ nm. After a long transient (hundreds of delay times τ), it evolved into the stable strange attractor shown in Fig. 10.

mode spectra. Usually, two-mode solutions are more stable than single-mode ones. It must be stressed that this transition, often dubbed ''single-mode to multimode switching,'' occurs within a chaotic regime and is a different phenomenon from the so-called coherence collapse [16,17]) which is also related to a broadening of the spectrum. The latter, in fact, is just the first appearance of chaos upon change of a bifurcation parameter, often accompanied by low-frequency

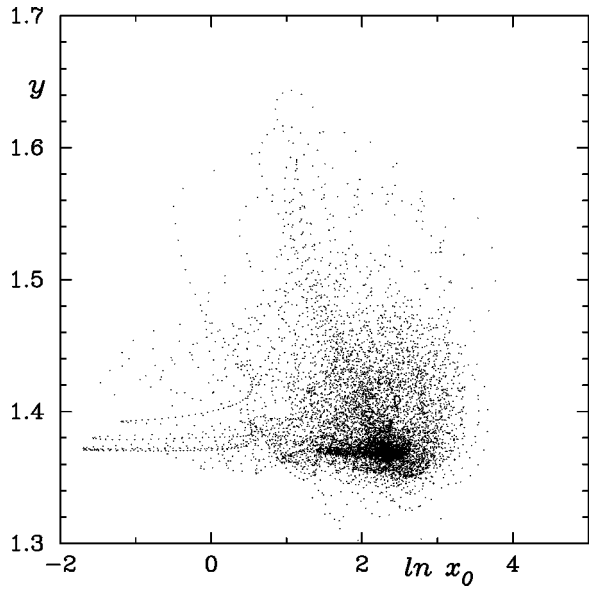

FIG. 10. Stable strange attractor observed at the same parameter values used in the computations of the orbit in Fig. 9. Notice the rare amplitude drops and the bursts in the carrier density.

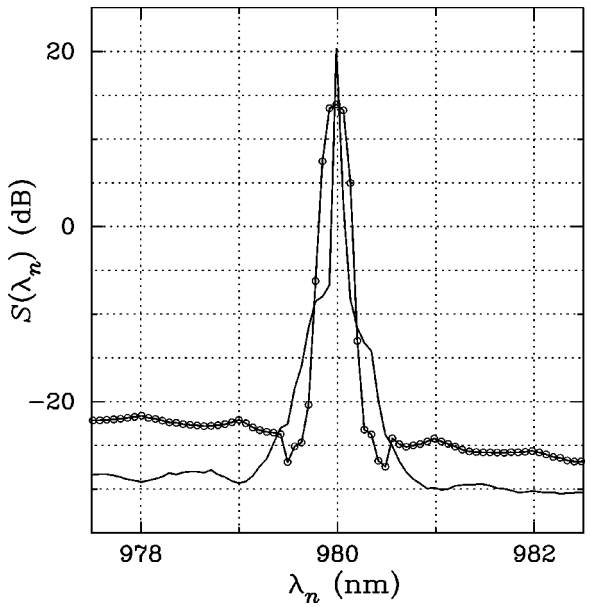

FIG. 11. Numerical optical spectra corresponding to the orbits of Figs. 9 (simple line) and 10 (line and circles): the former is narrow (single mode), while the latter is multimodal.

amplitude fluctuations, and is observed in single-mode models as well: after the onset of chaos, the derivative $\dot{\phi}$ also fluctuates chaotically and displaces the emission frequency ω [see Eq. (2.2)], so that a line broadening appears in the optical spectrum.

The coexistence of strange attractors, a phenomenon which is not observed in the low-feedback (Lang-Kobayashi) approximation, is documented in Figs. 12–14. The parameter values are $I=150$ mA, $L_{\text{ext}}=1$ m, $R_3=0.1$, and $\Delta\lambda=2$ nm. The larger attractor is of the Shilnikov type [32]: a fixed point, close to (3.3, 1.265) in this two-dimensional projection, has a two-dimensional stable manifold with complex-conjugate eigenvalues and a one-dimensional un-

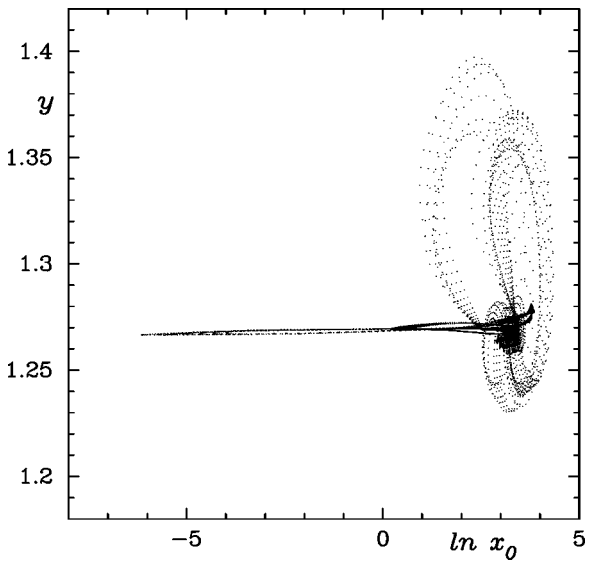

FIG. 12. Stable, Shilnikov-type strange attractor, computed at $I=150$ mA, $R_3=0.1$, $L_{\text{ext}}=1$ m, and $\Delta\lambda=2$ nm.

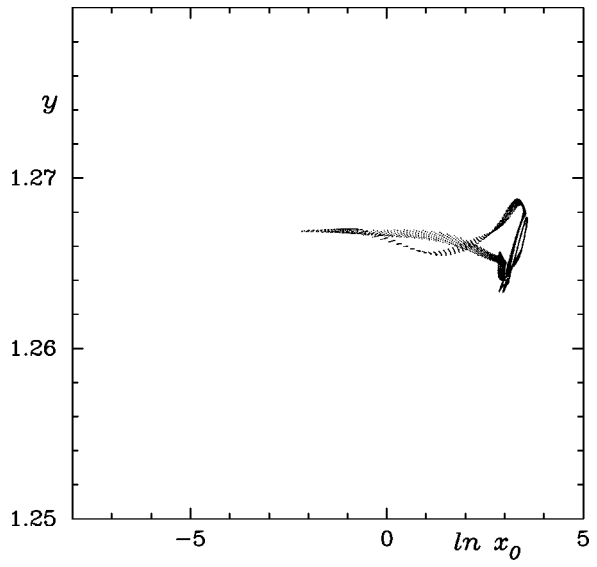

FIG. 13. Smaller stable attractor, observed at the same parameter values used in the computation of the solution in Fig. 12. Notice the different scales on the *y* axis.

stable manifold (nearly in the direction of constant *y*) with a real eigenvalue. The smaller attractor has a similar temporal evolution, with a twisted shape, but the Shilnikov structure is less clearly unfolded. In spite of their qualitatively different aspect, the two solutions correspond to nearly identical optical spectra. Since the coexistence of (possibly several) attractors, either all chaotic or not, is widespread in this system, it appears that the mere recording of optical spectra in the laboratory can hardly help classify the dynamical behavior in a precise way.

Finally, we briefly illustrate the transition between frequency-locked and either unlocked or partly locked con-

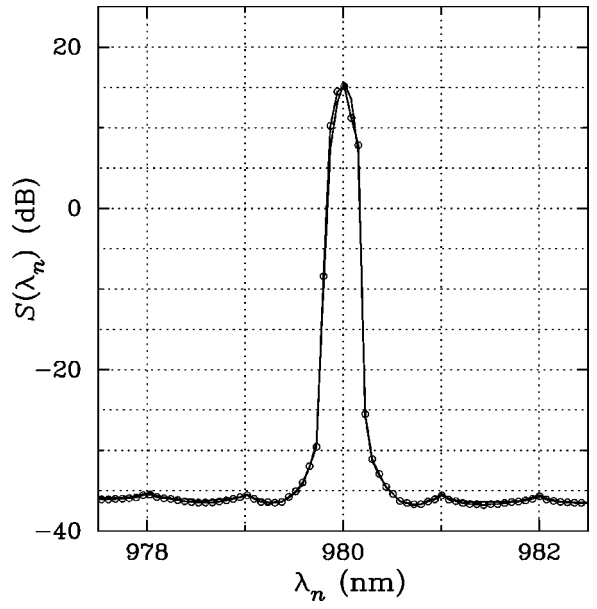

FIG. 14. Numerical optical spectra corresponding to the orbits of Figs. 12 (simple line) and 13 (line and circles). The graphs almost coincide.

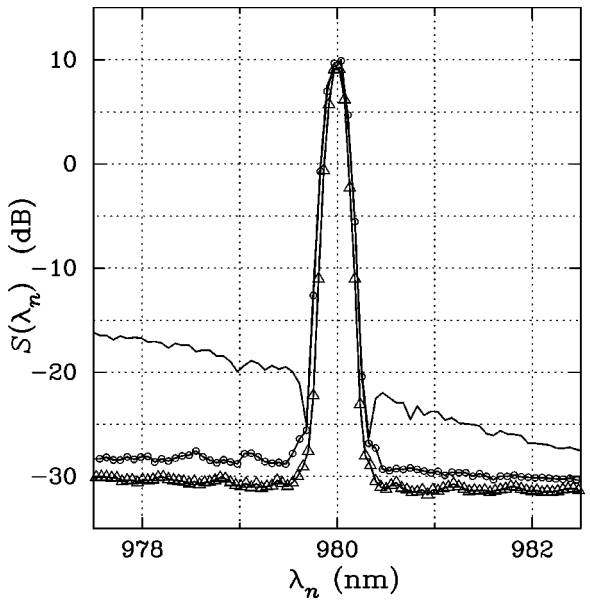

FIG. 15. Numerical optical spectra of generation-I (simple solid line and line with circles) and of generation-II (triangles) lasers, all computed under the same conditions ($I=60$ mA, $R_3=0.015$, $L_{\rm ext}=1$ m, and $\Delta\lambda=1.2$ nm). The first two alternate irregularly in time, with the device being mostly in the well-locked condition (circles).

dition in this laser setup. In Fig. 15, three optical spectra are shown. They have all been computed for $I=60$ mA, $R_3=0.015$, $L_{\rm ext}=1$ m, and $\Delta\lambda=1.2$ nm, but using lasers of different generations. The solid curve without symbols exhibits a partly locked spectrum of a generation-I laser which later evolves into an unlocked spectrum, in which emission occurs around the gain maximum (outside of the figure, on the left), and then returns to a well-locked situation, which is marked with circles. These states alternate irregularly in time, whereby the fully locked behavior is widely predominant. The third graph, marked with triangles, shows a perfectly locked state for a generation-II device which exhibits stable behavior in this parameter region. The different laser cavity length reflects in the different mode spacing (a 33% difference), which is clearly visible in the figure. This kind of instability is characterized by ample oscillations in the carrier density *y* (wider than those observed in Fig. 12), while possible intermissions of the phase-space trajectories into the low-amplitude regions are uninfluential. The attractors of the generation-II lasers for this parameter choice are smaller and more concentrated than those of generation-I devices, and are shifted towards lower carrier density. All these attractors are qualitatively similar to the one displayed in Fig. 10.

V. COMPARISON WITH THE EXPERIMENT

In this final section, we present experimental optical spectra and the corresponding time series in Figs. 16–21. The parameters values again correspond to typical frequency-stabilized pump lasers. The first two examples refer to a generation-I laser and the last four to a generation-II laser: the main differences between these devices are in the front-

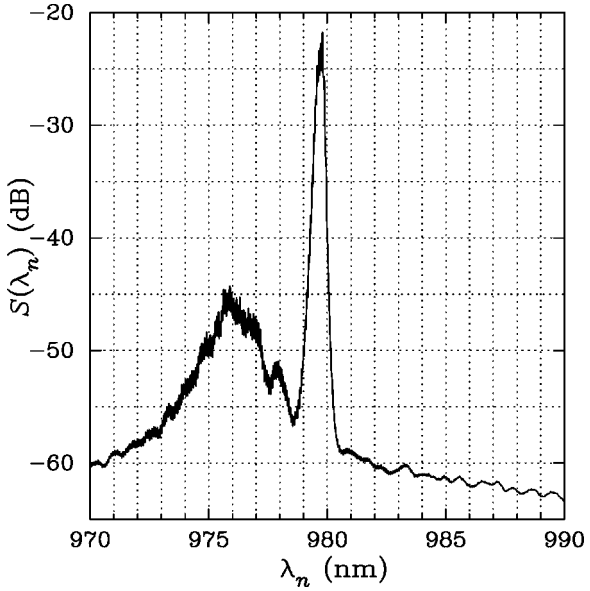

FIG. 16. Experimental optical spectra of generation-I lasers recorded at $I=60.4$ mA, $R_3=0.015$, $L_{\text{ext}}=1$ m, $\Delta\lambda=4$ nm, and $T=18.2$ °C.

facet reflectivity and in the cavity length, as mentioned above. Figure 16 clearly shows the main peak due to the reflection from the FBG and a side peak centered around the gain curve of the device. Notwithstanding the different parameter settings, this spectrum is comparable with the one displayed in Fig. 8. The dynamics, however, is clearly different. While Fig. 8 corresponds to a torus (Fig. 7), in the present example the motion is chaotic, as appears from the time series displayed in Fig. 17. Relatively frequent amplitude drops are visible: this is the phenomenon often referred to as ''low-frequency fluctuations.'' The strange attractor, which can be reconstructed via embedding, has a shape of the kind shown in Fig. 10. The limited time resolution of the measurements (5 ns) only allows to view the overall shape and apparent density of the attractors, but no clear details of the orbits. For this reason, no experimental attractors are shown.

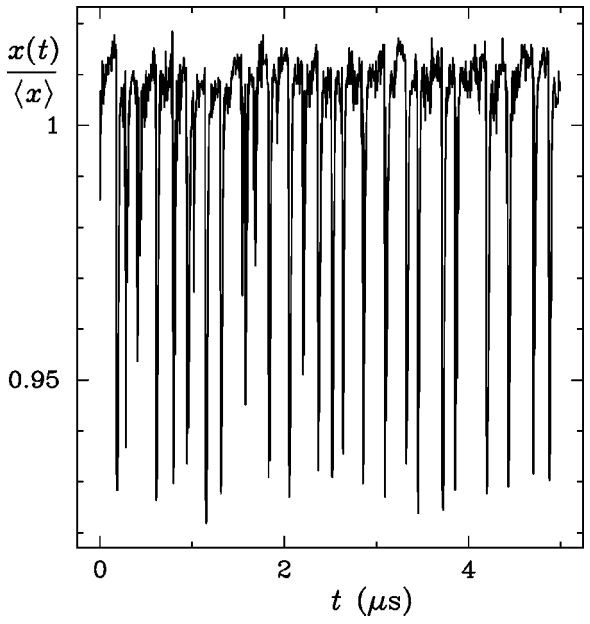

FIG. 17. Time-series of the total intensity $x(t)$, normalized to its average $\langle x\rangle$, vs time t, corresponding to the spectrum in Fig. 16: time is in units of 1 μs.

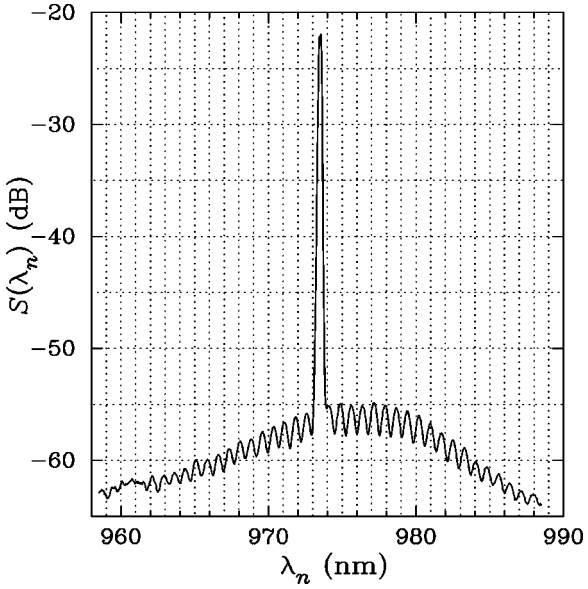

FIG. 18. Same as in Fig. 16, for a generation-II laser, recorded at $I=60.3$ mA, $R_3=0.03$, $L_{\text{ext}}=2$ m, $\Delta\lambda=1$ nm, and $T=25$ °C.

A different kind of amplitude drop is seen in the next example, Figs. 18 and 19, which demonstrates how a perfectly stable and locked optical spectrum can hide interesting dynamical behavior. The FBG central frequency is here $\lambda_{\text{Bragg}}=973.5$ nm.

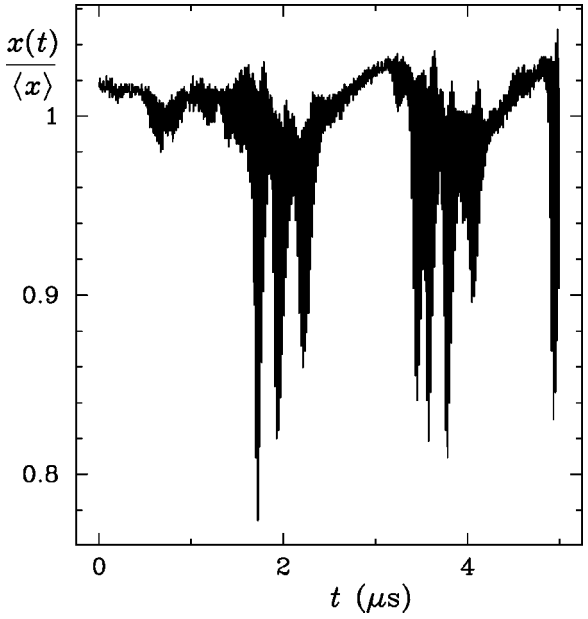

FIG. 19. Time series corresponding to the spectrum in Fig. 18, in analogy with Fig. 17.

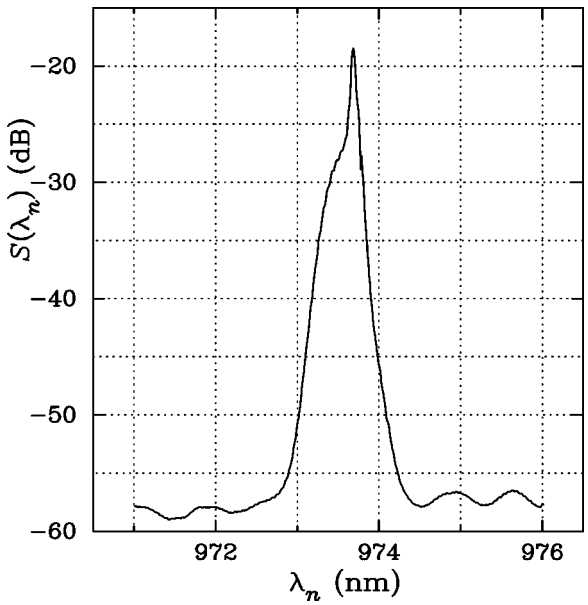

FIG. 20. Same as in Fig. 18, identical laser, recorded at $I = 450.1$ mA, $R_3 = 0.02$, $L_{\text{ext}} = 2$ m, $\Delta\lambda = 1$ nm, and $T = 25\,^{\circ}\text{C}$.

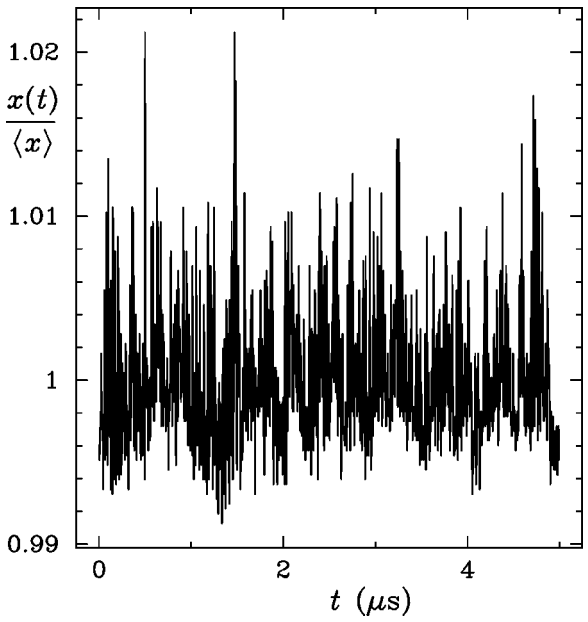

FIG. 21. Time series corresponding to the spectrum in Fig. 20.

Finally, a typical high-power optical spectrum is shown in Fig. 20. The corresponding time series is completely different from the previous ones: no low-frequency fluctuations occur, and the sequence has a ''random'' aspect. The attractor is apparently high dimensional. All of these features are well reproduced by model (3.3).

VI. CONCLUSIONS

We have studied the multimode dynamics of 980 nm pump lasers coupled with high-reflectivity, frequency-selective fiber-Bragg gratings, both numerically and experimentally. An improved set of rate equations, which allows one to treat high feedback levels, such as those usually employed in optical communication systems, has been presented. This type of frequency selection (stabilization) drives the system deeply in a chaotic regime. Within it, we have singled out a few particularly relevant solutions and the transitions that take place among them.

We pointed out that some of the latter and the alternation of frequency-locked and unlocked states do not have a counterpart in weak-feedback models, such as Lang-Kobayashi's. Moreover, the multimode system exhibits a richer phenomenology than single-mode ones. Narrow (possibly single-mode) optical spectra have been shown to appear when the trajectories visit certain regions of phase space, depending on the parameters of the system. The switching between multimode and narrow optical spectra, documented in Figs. 9–11, has been shown to correspond to transitions between chaotic and periodic attractors (either stable or destabilized by noise).

This is inherently different from the broadening of spectral lines associated with the low-frequency fluctuations that are commonly reported, primarily in single-mode systems, in connection with the term coherence collapse. The present study also casts light on this, often nebulously defined, concept. Indeed, broadening of the optical spectral lines is caused by the chaotic fluctuations of the phases which accordingly affect the values of the emission frequencies. Therefore, this phenomenon is just a manifestation of the chaotic nature of the system's trajectories.

Finally, the beneficial effect of chaos on multimode operation is reinforced in the sense that narrow-band spectra appear to correspond to small regions of phase-space which tend to shrink for generation-II lasers, since these achieve higher output power and, in turn, higher levels of chaos, with more compact attractors.

[1] F. Favre, D. LeGuen, and J.C. Simon, IEEE J. Quantum Electron. **QE-18**, 1712 (1982).
[2] K. Kikuchi and T. Okoshi, Electron. Lett. **18**, 10 (1982).
[3] J.O. Binder and G.D. Cormack, IEEE J. Quantum Electron. **25**, 2255 (1989).
[4] R. Lang and K. Kobayashi, IEEE J. Quantum Electron. **QE-16**, 347 (1980).
[5] C.H. Henry and R.F. Kazarinov, IEEE J. Quantum Electron. **QE-22**, 294 (1986).
[6] R.W. Tkach and A.R. Chraplyvy, J. Lightwave Technol. **LT-4**, 1655 (1986).
[7] The result is a ''delayed dynamical system,'' a kind of model which is the subject of active theoretical and experimental investigations [8–13].
[8] M.C. Mackey and L. Glass, Science **197**, 287 (1977).
[9] J.D. Farmer, Physica D **4**, 366 (1982).
[10] J. Mørk, B. Tromborg, and J. Mark, IEEE J. Quantum Electron. **28**, 93 (1992).

[11] J. Simonet, E. Brun, and R. Badii, Phys. Rev. E **52**, 2294 (1995).
[12] J. Mallet-Paret, J. Diff. Eqns. **125**, 385 (1996).
[13] G. Giacomelli and A. Politi, Physica D **117**, 26 (1998).
[14] M. Fujiwara, K. Kubuta, and R. Lang, Appl. Phys. Lett. **38**, 217 (1981).
[15] R. Ries and F. Sporleder, Proceedings of the Eighth ECOC, Cannes, France, 1982, p. 285.
[16] D. Lenstra, B.H. Verbeek, and A.J. Denoef, IEEE J. Quantum Electron. **QE-21**, 674 (1985).
[17] K. Petermann, *Laser Diode Modulation and Noise* (Kluwer, Dordrecht, 1991).
[18] M. Achtenhagen, S. Mohrdiek, T. Pliška, N. Matuschek, C.S. Harder, and A. Hardy, IEEE Photonics Technol. Lett. **13**, 415 (2001).
[19] G. Vaschenko, M. Giudici, J.J. Rocca, C.S. Menoni, J.R. Tredicce, and S. Balle, Phys. Rev. Lett. **81**, 5536 (1998); I. Wallace, D. Yu, R.G. Harrison, and A. Gavrielides, J. Opt. B: Quantum Semiclassical Opt. **2**, 447 (2000); E.A. Viktorov and P. Mandel, Phys. Rev. Lett. **85**, 3157 (2000); T.W. Carr, D. Pieroux, and P. Mandel, Phys. Rev. A **63**, 033817 (2001).
[20] In order to simplify the notation, the same symbol R_m is used for both the reflector and its reflectivity, as long as no misunderstanding arises. Then, $R_3=\max\{|r_3|^2\}$ denotes the peak reflectivity of the FBG.
[21] R. Kashyap, *Fiber Bragg Gratings* (Academic Press, San Diego, 1999).
[22] H. Rong-Qing and T. Shang-Ping, IEEE J. Quantum Electron. **25**, 1580 (1989).
[23] L. A. Coldren and S. W. Corzine, *Diode Lasers and Photonic Integrated Circuits* (Wiley, New York, 1985).
[24] C.H. Henry, IEEE J. Quantum Electron. **QE-18**, 359 (1982).
[25] The more general form $\Sigma_m \epsilon_{nm} P_m$ has also been used, with various choices of the matrix ϵ_{nm} such as $\epsilon_{nm}=\epsilon/(1+|n-m|)$. In the following, however, we only consider the diagonal form $\epsilon_{nm}=\epsilon\delta_{nm}$, which leads to expression (2.14).
[26] B. Schmidt, S. Mohrdiek, C. Harder, in *Optical Fiber Telecommunications IV-A*, edited by I. P. Kaminov and T. Li (Academic Press, San Diego, 2002), p. 563; B. Schmidt, S. Pawlik, B. Mayer, S. Mohrdiek, I. Jung, B. Sverdlov, N. Lichtenstein, N. Matuschek, and C. Harder, in Proceedings of the Optical Fiber Communication Conference, Anaheim, CA, 2002, p. 702.
[27] B. Zhao, T.R. Chen, S. Wu, Y.H. Zhuang, Y. Yamada, and A. Yariv, Appl. Phys. Lett. **62**, 1591 (1993).
[28] D.T. Cassidy, J. Appl. Phys. **56**, 3096 (1984).
[29] B.W. Hakki and T.L. Paoli, J. Appl. Phys. **46**, 1299 (1975).
[30] B. Tromborg, J.H. Osmundsen, and H. Olesen, IEEE J. Quantum Electron. **QE-20**, 1023 (1984).
[31] T. Sano, Phys. Rev. A **50**, 2719 (1994).
[32] L.P. Shilnikov, Sov. Math. Dokl. **6**, 163 (1965); Math. USSR Sb. **10**, 91 (1970).